ZZ-interaction-free single-qubit-gate optimization in superconducting qubits

Shu Watanabe ●,[1,*] Yutaka Tabuchi,[2] Kentaro Heya,[2,†] Shuhei Tamate,[2] and Yasunobu Nakamura ●[1,2]

[1]*Department of Applied Physics, Graduate School of Engineering, University of Tokyo, 7-3-1 Hongo, Bunkyo-ku, Tokyo 113-8656, Japan*
[2]*RIKEN Center for Quantum Computing, Wako, Saitama 351-0198, Japan*

Overcoming the issue of qubit-frequency fluctuations is essential to realizing stable and practical quantum computing with solid-state qubits. Static *ZZ* interaction, which causes a frequency shift of a qubit depending on the state of neighboring qubits, is one of the major obstacles to integrating fixed-frequency transmon qubits. Here we propose and experimentally demonstrate *ZZ*-interaction-free single-qubit-gate operations on a superconducting transmon qubit by utilizing a semianalytically optimized pulse based on a perturbative analysis. The gate is designed to be robust against slow qubit-frequency fluctuations. The robustness of the optimized gate spans a few megahertz, which is sufficient to suppress the adverse effects of the *ZZ* interaction. Our result paves the way for an efficient approach to overcoming the issue of *ZZ* interaction without any additional hardware overhead.

I. INTRODUCTION

Practical quantum information processing requires high-fidelity and stable quantum gate operations. In the platforms with solid-state qubits such as superconducting qubits and semiconductor spin qubits, a qubit frequency often drifts or fluctuates due to the influence of surrounding environments. The changes of qubit frequencies cause infidelity of their gate operations.

Previous studies reported that two-level systems (TLSs), charge noise, and parity switching are sources of frequency fluctuations in superconducting qubits [1–5], which cause dephasing and gate errors due to detuning. Most importantly, the residual *ZZ* interaction between qubits, which changes the qubit frequency of interest depending on the neighboring qubit states, is an obstacle to integrating superconducting qubits. Multipath couplings [6,7], tunable couplers [8–10], weakly driven couplers [11], simultaneous ac Stark effects [12,13], and utilizing low-degree graphs [14] have been proposed as countermeasures against the residual *ZZ* interaction.

To achieve high-fidelity quantum control in the presence of a device instability, such as a qubit-frequency drift, a robust control scheme against the fluctuations is required. The concept of dynamically corrected gates [15] is known for its ability to realize fluctuation-resilient quantum control. It was first introduced in nuclear magnetic resonance as a generalization of composite pulses [16–19]. We can regard the dynamically corrected optimal gates as an extension of the spin echoes or dynamical decoupling [20], given that the control pulse refocuses faulty qubit dynamics due to fluctuating sources. Using a perturbative analysis with the Magnus expansion [21], the dynamical-correction-based gate designs are free from sampling a large number of data sets of error strength unlike fully numerical robust quantum-gate designs [22–24]. Incorporating the concept of dynamically corrected gates into quantum optimal control theory [25–28] enables one to analytically [29,30] or semianalytically [31–35] design robust quantum gates with smooth pulses. Beside dynamically corrected gates, we also note that robust quantum-gate designs using deep reinforcement learning [36] have been proposed for solid-state qubits. It is also recognized that the echoed cross resonance [37,38] and the rotary pulses [38,39] are effective in mitigating the frequency shift due to the *ZZ* interaction during the execution of two-qubit cross-resonance gates between fixed-frequency transmon qubits.

In this paper we mitigate the negative impact of the residual *ZZ* interaction between neighboring qubits on single-qubit gates by semianalytically optimizing the pulse waveform based on dynamical correction. Our pulse optimization emphasizes the practicality of the pulse for use in experiments. By properly choosing the waveform ansatz, we avoid impractical pulse shapes with a large derivative. Another feature of our method lies in its universality. The optimal waveform is determined independently of the individual qubit parameters, and the experimental protocol for gate calibration is as simple as those for conventional waveforms such as Gaussian. This approach for *ZZ*-interaction suppression is distinct from other existing methods mentioned above since it requires no hardware overheads, such as additional circuit elements, flux bias lines, or drive channels.

II. DYNAMICALLY CORRECTED GATES

Our strategy for optimizing a single-qubit gate robust against detuning is based on the concept of dynamically corrected

---

*watanabe@qipe.t.u-tokyo.ac.jp
†Present address: IBM Quantum, IBM Thomas J. Watson Research Center, Yorktown Heights, New York 10598, USA.

012616-1

corrected gates (DCGs) [15,31–35]. In the DCG-based synthesis, we begin by classifying the Hamiltonian of the system into an unperturbed term $\hat{H}_0(t)$ and an error term $\hat{H}_{\text{error}}(t)$ as

$$\hat{H}_{\text{total}}(t) = \hat{H}_0(t) + \hat{H}_{\text{error}}(t). \qquad (1)$$

With the classification, we separate the overall time propagator $\hat{U}_{\text{total}}(t)$ into nonperturbative dynamics $\hat{U}_0(t)$ and faulty dynamics $\hat{U}_I(t)$ as $\hat{U}_{\text{total}}(t) = \hat{U}_0(t)\hat{U}_I(t)$, where we define

$$\dot{\hat{U}}_0(t) = -i\hat{H}_0(t)\hat{U}_0(t) \qquad (2)$$

and

$$\dot{\hat{U}}_I(t) = -i\hat{H}_I(t)\hat{U}_I(t) \qquad (3)$$

by using the toggling-frame Hamiltonian

$$\hat{H}_I(t) = \hat{U}_0^\dagger(t)\hat{H}_{\text{error}}(t)\hat{U}_0(t). \qquad (4)$$

It is useful to approximate the faulty dynamics over a time interval T by defining the effective time-independent average Hamiltonian

$$\hat{U}_I(t) \simeq \exp(-i\bar{\hat{H}}T). \qquad (5)$$

The average Hamiltonian can be expressed by the Magnus expansion [20,21]

$$\bar{\hat{H}} = \sum_n \bar{\hat{H}}^{(n)}. \qquad (6)$$

The lowest- and second-lowest orders of the Magnus expansion are given by

$$\bar{\hat{H}}^{(1)} = \frac{1}{T}\int_0^T dt\, \hat{H}_I(t), \qquad (7)$$

$$\bar{\hat{H}}^{(2)} = \frac{-i}{2T}\int_0^T \int_0^t dt\, dt'[\hat{H}_I(t), \hat{H}_I(t')]. \qquad (8)$$

The precision of the approximation is guaranteed when $\|\hat{H}_{\text{error}}T\| \ll 1$. By designing the unperturbed term $\hat{H}_0(t)$ so that the average Hamiltonian $\bar{\hat{H}}$ vanishes, we can consider that the effect of the error term on the system's time evolution is stroboscopically negligible at time T. Since the Magnus expansion is defined with the integrals, whether the average Hamiltonian is zero or not is independent of the norm of the error terms and depends only on the functional form of $\hat{H}_{\text{error}}(t)$ and $\hat{H}_0(t)$.

Under a single-qubit control drive at the qubit frequency and with the rotating-wave approximation, the unperturbed term $\hat{H}_0(t)$ becomes

$$\hat{H}_0(t) = \Omega_x(t)\frac{\hat{\sigma}_x}{2} + \Omega_y(t)\frac{\hat{\sigma}_y}{2}. \qquad (9)$$

Therefore, a dynamically corrected single-qubit gate can be designed in two steps: First, we decide which errors to gain robustness against, and second, we optimize the waveforms $\Omega_x(t)$ and $\Omega_y(t)$ so that the average Hamiltonian in the toggling frame vanishes. As discussed above, the vanishing of the average Hamiltonian depends only on the functional form of the error term and the drive waveform, not on the norm of the error terms. In other words, by using the toggling frame and average Hamiltonian, we can naturally acquire robustness against the amplitude of the error. Therefore, our strategy is to find through a numerical optimization the optimal control

waveforms $\Omega_x(t)$ and $\Omega_y(t)$ that simultaneously satisfy two conditions

$$\hat{U}_0(T) = \hat{U}_{\text{target}} \qquad (10)$$

and

$$\bar{\hat{H}} = 0, \qquad (11)$$

where $\hat{U}_{\text{target}}$ is the unitary that expresses the target gate. The former condition aims to achieve the desired gate operation and the latter aims to acquire robustness against errors.

III. PULSE SYNTHESIS

We synthesize an optimal waveform of a single-qubit $X_{\pi/2}$ gate robust against the time-independent or slowly varying detuning of the qubit frequency modeled as $\hat{H}_{\text{error}} = \xi\hat{\sigma}_z/2$. Because of the noncommutativity of $\hat{\sigma}_z$ and $\hat{\sigma}_x$, the in-phase component of the drive $\Omega_x(t)$ is sufficient for mitigating the detuning error that we focus on. This simplification reduces the number of optimization parameters and accelerates the convergence. By using the unitary operator $\hat{U}_0(t) = \mathcal{T}\exp[-i\int_0^t \Omega_x(\tau)d\tau\frac{\hat{\sigma}_x}{2}]$, where $\mathcal{T}$ stands for the time-ordered product, the error Hamiltonian on the toggling frame $\hat{H}_I(t) = \hat{U}_0^\dagger(t)\hat{H}_{\text{error}}\hat{U}_0(t)$ is derived as

$$\hat{H}_I(t) = \xi\left(\cos\Theta(t)\frac{\hat{\sigma}_z}{2} + \sin\Theta(t)\frac{\hat{\sigma}_y}{2}\right), \qquad (12)$$

where $\Theta(t) = \int_0^t \Omega_x(\tau)d\tau$. We then approximate the faulty dynamics introduced by the error term using the Magnus expansion based on the average Hamiltonian theory [40]. The exact expression of the Magnus expansion is found in Sec. II. The deviation of the dynamics from the ideal one can be neglected when the drive is designed such that the error Hamiltonian vanishes stroboscopically under the truncation in the Magnus expansion. We numerically optimize the drive waveforms $\Omega_x(t)$ by adopting a waveform ansatz expressed as the product of polynomials and cosine

$$\Omega_x(t) = \sum_n a_n^{(x)}\left(t - \frac{T}{2}\right)^n \cos^2\left[\frac{\pi}{T}\left(t - \frac{T}{2}\right)\right], \qquad (13)$$

where $\{a_n^{(x)}\}$ are the parameters to be optimized and T is the gate length. We suppose that the pulse of Eq. (2) is applied during the period $0 \leqslant t \leqslant T$, and otherwise $\Omega_x(t) = 0$. This ansatz forces the pulse and its derivative to start and end at zero. Considering the use of the derivative removal by adiabatic gate (DRAG) correction, as discussed later, this is essential to enhance the practicality of the optimized gate in experiments since we can minimize the probability of a nonadiabatic transition. The careful choice of the waveform ansatz enables us to realize relatively fast and high-fidelity single-qubit gates compared to the previous work [35]. The pulse optimization is executed to satisfy two conditions: (i) The overall time evolution of the qubit is identical to the target gate and (ii) the error Hamiltonian on the toggling frame is averaged to zero.

The optimization problem is to minimize a cost function $C = 1 - \frac{1}{2}|\text{Tr}[\hat{U}_{\text{target}}^\dagger\hat{U}_0(T)]|$ subject to $\bar{\hat{H}} = 0$. We treat this constrained optimization problem as a multiobjective

TABLE I. Parameters of the optimal $X_{\pi/2}$ pulse robust against detuning.

n	$a_n^{(x)}$
0	0.31831
2	-0.00515

optimization problem to minimize

$$C_{\text{all}}\big(\{a_n^{(x)}\}\big) = w C_{\text{fidelity}}\big(\{a_n^{(x)}\}\big) + (1-w) C_{\text{robust}}\big(\{a_n^{(x)}\}\big), \tag{14}$$

where the parameters $\{a_n^{(x)}\}$ are defined as Eq. in (2) to parametrize the shape of the X-control pulse. We define two parts of the cost function as

$$C_{\text{fidelity}}\big(\{a_n^{(x)}\}\big) = \left|\Theta(T) - \frac{\pi}{2}\right| \tag{15}$$

and

$$C_{\text{robust}}\big(\{a_n^{(x)}\}\big) = \frac{1}{T}\left(\left|\int_0^T \cos\Theta(t)\mathrm{d}t\right| + \left|\int_0^T \sin\Theta(t)\mathrm{d}t\right|\right), \tag{16}$$

where $\Theta(t) = \int_0^t \Omega_x(\tau)\mathrm{d}\tau$ is used for simplification. Note that Eq. (16) characterizes the L_1-norm of the lowest-order average Hamiltonian calculated from Eq. (1). These two parts of the cost function correspond to the conditions (10) and (11) explained above, respectively. The weight factor w in Eq. (14), which determines the balance between maximizing fidelity and minimizing the norm of the average Hamiltonian, is deliberately chosen between 0 and 1 to achieve the desired optimization. The value of w is set to be 0.999 in our optimization since we empirically find that it is more likely to make both terms in the cost function (14) smaller when w is close to 1.

The parameters of the synthesized waveform expressed with the ansatz (2) are listed in Table I. Using higher-degree polynomials increases the freedom of expression of the waveform but likely results in a larger derivative of the waveform, which may increase the probability of nonadiabatic transitions. In addition, instruments impose bandwidth limitations in experiments. We use polynomials up to the second order ($n \leqslant 2$). We also fix the first-order coefficient ($n = 1$) to zero to synthesize a time-symmetric waveform, which is not mathematically essential. The gate duration T is chosen to be 40 ns. The initial guess of the parameters are $a_0^{(x)} = \pi/T$ and $a_n^{(x)} = 0$ for $n \neq 0$. We utilize the limited-memory Broyden-Fletcher-Goldfarb-Shanno. method [41] for the optimization. The numerical integrals necessary for the cost evaluation are performed by dividing 1 ns into 64 equal fractions.

It is worth mentioning that since the cost function (14) does not include any information about the system, such as the qubit frequency or magnitude of the frequency drift, the obtained values in Table I are universal and commonly applicable to any qubit that can be expressed by this model as long as the convergence condition for the Magnus expansion, $\|\xi T\| \ll 1$, is fulfilled.

IV. EXPERIMENT

We use fixed-frequency transmon qubits Q0 and Q1 in the experiments. For detailed information on the whole device and the qubits used in the experiments, see Appendix A.

First, we use the target qubit Q0 to evaluate the gate fidelity and the robustness against detuning error. We set the pulse length T to be 40 ns and construct the optimized pulse with the polynomials up to $n = 2$. We also apply the DRAG with Y-only correction, mentioned in Ref. [42], since we empirically find through numerical simulations that the impact of the use of Y-only DRAG on the robustness of the optimized gate against the detuning is small. We emphasize that the optimized waveform is universal in the sense that it is independent of the individual qubit parameters; we only need to experimentally calibrate the absolute pulse amplitude and DRAG weight for each qubit. Thus, the calibration protocol is as simple as the one for conventional waveforms like Gaussian. It should also be noted that the maximum amplitude of the optimal waveform is about four times larger than that of the Gaussian waveform for the identical gate length, as shown in Fig. 1(a). In general, the more degrees we include in the polynomials in the ansatz, the more robustness we gain. However, the time derivative of the waveform becomes larger and nonadiabatic transitions become more significant. This tradeoff is a factor that needs to be considered when one seeks to realize fast and robust quantum gates. An analysis of leakage error to the higher excited state is shown in Sec. V.

Next we evaluate the gate fidelity and robustness of the optimized pulse based on randomized benchmarking (RB) [43,44]. See Appendix B for the calibration details. Figures 1(a) and 1(b) are the calibrated waveform and the result of interleaved randomized benchmarking (IRB), respectively. In the RB sequence, all single-qubit Clifford gates consist of two $X_{\pi/2}$ gates and three virtual-Z gates [45]. The gate fidelity measured by the IRB is $99.81 \pm 0.02\%$. We note that this fidelity is mainly limited by the coherence of the qubit. The energy relaxation time T_1 and the echo dephasing time T_2 of Q0 are 13 and 10 μs, respectively. The theoretical coherence limit of the gate fidelity is numerically obtained using measured T_1 and T_2. We also note that the numerically obtained error rate per gate of the optimized waveform without decoherence is less than 10^{-6}, which implies that there is significant room to achieve much better fidelity by improving the coherence time. In Fig. 2 we show the error rate per gate (EPG) versus drive detuning to investigate the robustness of the optimized waveform against the detuning. As our qubit is a fixed-frequency qubit, we detune the frequency of the driving pulse instead of the qubit frequency. Here we apply the intentional detuning only to the interleaved gates. The robustness is compared with the widely used DRAG-optimized Gaussian pulse with the same pulse length of 40 ns and shows a significant improvement. The increase in EPG is well suppressed even with a few-megahertz detuning. The range of robustness is consistent with the condition $|\xi T| \ll 1$, which justifies the lowest-order Magnus expansion.

Considering that the designed gate maintains high fidelity over the wide bandwidth and that the typical magnitude of frequency drift due to TLSs and parity switching in superconducting transmon qubits is at most an order of megahertz
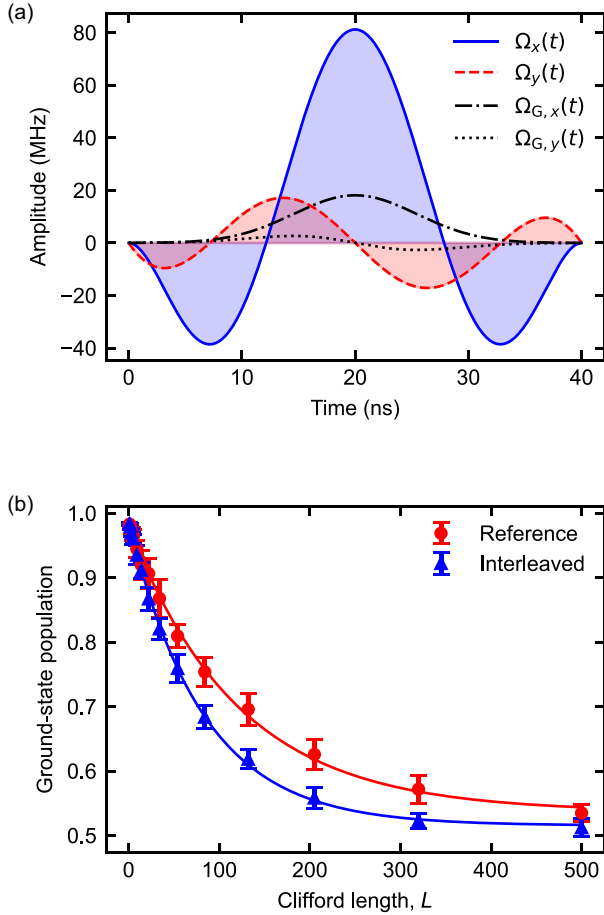
FIG. 1. (a) Optimized waveform $\Omega_x(t)$ (blue solid line) for the $X_{\pi/2}$ gate with calibrated DRAG correction $\Omega_y(t)$ (red dashed line). The real (x) and imaginary (y) parts of the Gaussian waveform $\Omega_{G,x}(t)$ with calibrated DRAG correction $\Omega_{G,y}(t)$ for the same gate are shown as black dash-dotted and dotted lines, respectively. (b) Interleaved randomized benchmarking of the $X_{\pi/2}$ gate using the optimal waveform at zero detuning. The plot is averaged over 40 random Clifford sequences per point. The measured error rate per gate is $1.9(2) \times 10^{-3}$.

[1,3–5], such broadband quantum gates can be an effective countermeasure to the degradation of control fidelity due to these slow fluctuations. Although transmon qubits are generally insensitive to the charge noise, it cannot be ignored when one implements quantum gates in noncomputational spaces such as $|e\rangle - |f\rangle$. Such control has recently been found useful for an efficient decomposition of Toffoli gates on qutrits [46,47]. Aside from superconducting qubits, another platform that can benefit from this optimized gate robust against detuning is semiconductor spin qubits. In silicon-based spin qubits, it is reported that the magnitude of slow drift in the qubit frequency is on the order of hundreds of kilohertz [48,49]. In addition, it is commonly known that the slow dynamics of nuclear spin bath affects the energy splitting of an electron spin via hyperfine interaction. Maintaining control fidelity under such frequency fluctuations is a prerequisite in quantum computing.

Next we study the impact of the residual ZZ interaction on the synthesized optimal single-qubit gate, using a spectator
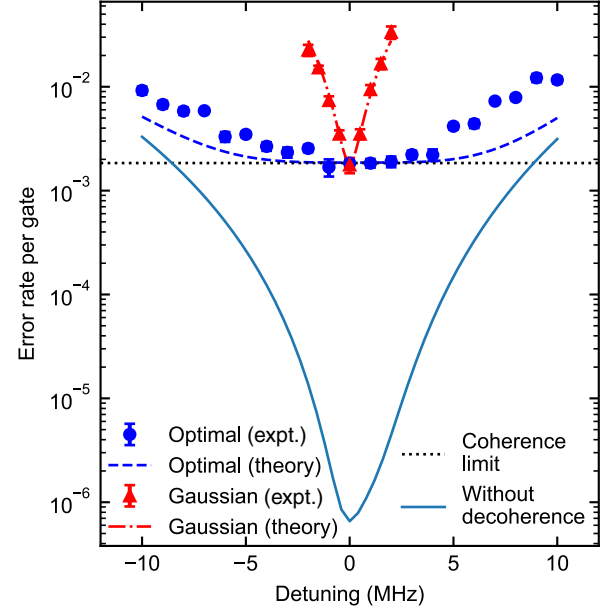

FIG. 2. Error rate per gate extracted from IRB versus drive detuning for the $X_{\pi/2}$ gate with the optimized (blue circles) and Gaussian (red triangles) waveforms with the theoretical predictions (dashed line for the optimal waveform and dash-dotted line for the Gaussian waveform). The solid line represents the theoretical limit to the gate error with infinite coherence times. The dotted line represents the theoretical coherence limit to the gate error.

qubit Q1 which is capacitively coupled to the target qubit Q0, as shown in Appendix A. Under the ZZ interaction with a spectator qubit, $\hat{H}_{\text{error}}$ is expressed as

$$\hat{H}_{\text{error}} = \xi_{ZZ} \frac{\hat{\sigma}_{z0} \otimes \hat{\sigma}_{z1}}{2}. \tag{17}$$

Here $\hat{\sigma}_{z0}$ and $\hat{\sigma}_{z1}$ are the Pauli-Z operators of the target and the spectator qubits, respectively, and ξ_{ZZ} denotes the ZZ coupling strength in between. Assuming that the state of the adjacent qubit is unchanged during the gate execution, we can reduce $\hat{H}_{\text{error}}$ to a frequency shift of the target qubit

$$\hat{H}_{\text{error}} = \chi \frac{\hat{\sigma}_{z0}}{2}, \tag{18}$$

where $\chi = \pm\xi_{ZZ}$. Note that this expression scales when the number of adjacent qubits increases if we assume that the states of all the adjacent qubits are unchanged. In the present device, the ZZ interaction ξ_{ZZ} between Q0 and Q1 is $2\pi \times 0.73$ MHz. Since our single-qubit gate length T is 40 ns, satisfying $|\chi T| \ll 1$, the legitimacy of the approximation with the lowest-order Magnus expansion is guaranteed.

We incorporate an RB-like methodology to quantify the impact of the spectator error. In the sequence, we run the standard IRB on the target qubit. In addition, we randomly apply single-qubit X_{π} pulses to the spectator qubit in synchronization with the reference Clifford gate to the target qubit. By averaging the result over a sufficiently large number of samplings, the spectator qubit's expectation value right before the $X_{\pi/2}$ pulse on the target qubit is averaged to $\overline{\langle\hat{\sigma}_z\rangle} = 0$. The deviation of the fidelity measured with this averaging from the one measured without operation to the spectator qubit shows the influence of the changes of the spectator's state, that is,
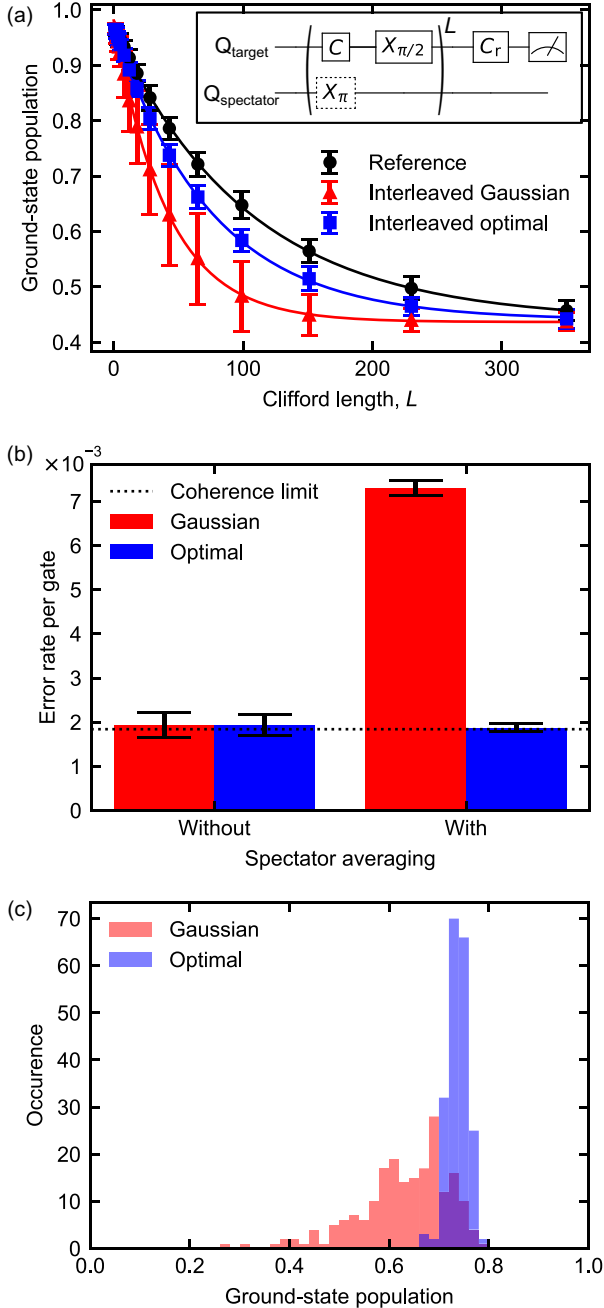
FIG. 3. (a) Interleaved randomized benchmarking with spectator averaging for Gaussian and optimal waveforms. The plot is averaged over 200 random Clifford sequences and 2000 shots per point. The gate schematic is shown in the inset. (b) Comparison of the error rates per gate with and without averaging the state of the spectator qubit. The dotted line indicates the coherence limit to the EPG. (c) Distributions of ground-state population for the Gaussian and optimal waveforms for Clifford length $L = 43$ in the spectator-averaging RB.

the impact of the residual ZZ coupling. In the following, this technique is referred to as spectator-averaging RB. The gate schematic is shown in the inset of Fig. 3(a).

Figure 3(a) shows the results of spectator-averaging RB for the optimal and Gaussian waveforms. The comparison of error rates with and without the spectator averaging shows that the

averaging significantly affects the fidelity of the Gaussian $X_{\pi/2}$ gate, as shown in Fig. 3(b). The EPG with spectator averaging is about four times worse than that without averaging. On the other hand, when the optimal waveform is employed, the EPG with spectator averaging is $1.9(1) \times 10^{-3}$, which is almost equal to the EPG obtained with the standard IRB. Figure 3(c) shows the distributions of the ground-state population after applying 43 Clifford gates in the spectator-averaging RB for the Gaussian and optimal waveforms, respectively. We observe a significantly larger spread in the distribution for the Gaussian waveform than the optimal one. The asymmetric shape of the distribution for the Gaussian gate is a consequence of the systematic error [50,51], which in this case is the spectator-dependent phase error due to the ZZ interaction. On the other hand, the relatively small spread in the distribution for the optimized gate indicates that it is insensitive to such phase error. Therefore, the optimized gate robust to detuning can reduce the negative impact of the ZZ interaction between the target and spectator qubits. As the magnitude of the ZZ interaction between qubits in typical transmon integrated circuits is several tens or hundreds of kilohertz [11,12] and the optimized gate has broadband robustness over a few megahertz of detuning, the scheme should work even when the number of adjacent qubits increases and the target qubit is exposed to ZZ interactions from them. The robustness contributes to the architectures with high qubit connectivity, including square lattices, while other issues, such as frequency collisions and two-qubit gates, remain. Since this implementation of a robust quantum gate does not require any additional wiring, circuit element, or drive channel, it serves as an alternative approach to tackling the issue of ZZ interaction.

Furthermore, the single-qubit gate robust to ZZ interaction is potentially useful for quantum computation scheme controlling always-on internal interactions through decoupling and selective recoupling [52–55]. The X gates are necessary for decoupling and recoupling sequences, which are not trivial under always-on coupling. Our optimized gate robust to ZZ interaction can be applied to implement high-fidelity X gates in such architectures.

V. LEAKAGE ANALYSIS

We evaluate the leakage error to the second excited state by leakage randomized benchmarking (LRB) [56]. The pulse sequence of LRB is the same as standard RB. We fit the population of the second excited state averaged over 40 random Clifford sequences as a function of the sequence length L to the decay model $p_2(L) = Ap^L + B$. The leakage rate per gate (LPG) is then computed as

$$l = B(1 - p)/2 \qquad (19)$$

since all single-qubit Clifford gates can be represented by two $X_{\pi/2}$ gates and three virtual-Z gates. In Fig. 4 we show LRB curves for the Gaussian and optimal waveforms. The LPGs measured by LRB are $1.3(1) \times 10^{-4}$ and $2.0(2) \times 10^{-4}$ for the Gaussian and optimal waveforms, respectively. On the other hand, numerically obtained LPGs are 1.3×10^{-4} and 1.5×10^{-4} for the Gaussian and optimal waveforms, respectively. The optimal waveform induces slightly more leakage to the noncomputational state than the simulation. We suppose
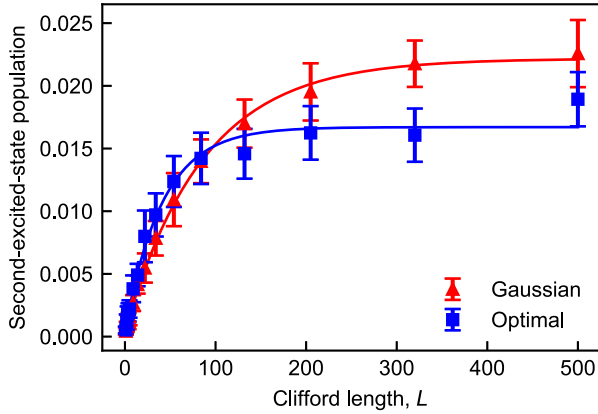
FIG. 4. Leakage randomized benchmarking of the $X_{\pi/2}$ gate using the Gaussian and optimal waveforms. The plot is averaged over 40 random Clifford sequences per point. The measured leakage rate per gate is $1.3(1) \times 10^{-4}$ and $2.0(2) \times 10^{-4}$ for the Gaussian and optimal waveforms, respectively. The solid lines represent the fits to the decay model.

that this is because of the influence of surrounding qubits that is not included in the simulation. We also obtain the lower bound on the LPG due to finite-temperature heating [57] by numerical simulation. Using measured T_1 and T_2 and the thermal excitation rate of the qubit, we calculate the lower bound as 1.3×10^{-4}. Furthermore, we simulate the LPG of the optimal waveform without decoherence. The obtained LPG without decoherence is less than 10^{-6}, implying that the leakage error would not limit the gate fidelity until the coherence time becomes by far longer. Therefore, although the experiment shows that the optimal waveform induces slightly more leakage to the noncomputational state than the Gaussian waveform of the same length, the leakage error is basically dominated by incoherent state transfer due to finite temperature and not limiting the gate fidelity.

VI. CONCLUSION

In this paper we proposed and experimentally demonstrated suppression of the adverse effect of ZZ interaction on single-qubit gates in transmon qubits using a semianalytically optimized waveform. We optimized the pulse waveforms to obtain robustness by utilizing dynamically corrected gates. Our pulse optimization emphasized the practicality of the pulse for use in experiments. By properly choosing the waveform ansatz, we avoided impractical pulse shapes with a large derivative or discontinuity. Our approach is distinct from other existing methods for mitigating the ZZ interaction, such as tunable or multipath couplers and simultaneous ac Stark effects, since it requires no additional circuit elements, wiring, or drive channels.

The error rate per gate of our optimized single-qubit gate is $1.9(2) \times 10^{-3}$, which is mainly limited by decoherence of the qubit. The error rate per gate remains unchanged even under a few megahertz of detuning.

The broadband robustness of the optimized gate was exploited to mitigate ZZ interaction during single-qubit gate operation. Using a qubit pair with a ZZ interaction of 0.73 MHz, we demonstrated significant improvement in the gate fidelity in comparison to the Gaussian waveform.

Our results pave the way for hardware-efficient ZZ-interaction-free quantum control in superconducting qubits. It also serves as a countermeasure against the issue of frequency fluctuations in quantum computation based on solid-state qubits.

APPENDIX A: EXPERIMENTAL APPARATUS

The device studied in this work consists of 16 qubits arranged in a 4×4 square lattice. The schematic and connectivity of the device are shown in Fig. 5(a). The experiments are run on two of the qubits, Q0 and Q1. Individual qubit parameters are listed in Table II. We treat Q0 as the target qubit and Q1 as the spectator qubit. During the experiments, other qubits are not controlled or measured. The qubits are dispersively read out through coplanar waveguide resonators with Purcell filters [58], and the readout is frequency multiplexed for four qubits in one unit. We utilize an impedance-matched Josephson parametric amplifier [59,60] for the qubit readout.

APPENDIX B: CALIBRATION

We apply the *Y*-only DRAG presented in Ref. [42] to suppress unwanted effects due to the presence of noncomputational states. We first roughly estimate the pulse amplitude for the $X_{\pi/2}$ gate as shown in Fig. 6(a). We select an amplitude that results in a ground-state population closest to 0.5 after the pulse is applied. Although the amplitude-population curve should be cosinelike, this is not the case here. We suppose this is because when strongly driven, the unwanted interaction is induced between the target and surrounding qubits. We repeat the DRAG-weight and pulse-amplitude calibrations alternately until the optimal condition remains constant. In Fig. 6(b) we show the gate schematic for calibrating the DRAG weight, which is based on Ref. [61]. In the pulse sequence, we apply $(X_{\pi/2} \, X_{-\pi/2})^n$ to the initial state $(|0\rangle - i|1\rangle)/\sqrt{2}$ so that the phase error is amplified and then measure $\langle \pm \sigma_x \rangle$. We run this pulse sequence with sweeping the DRAG weight to determine the optimal point
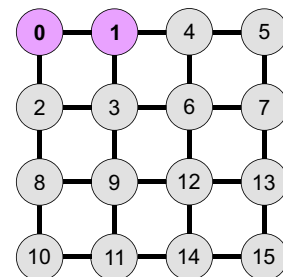

FIG. 5. Schematic of the 16-qubit square lattice. The qubits used in the experiments are shaded in purple.

TABLE II. Summary of qubit parameters.

Parameter	Q0	Q1
qubit frequency $\omega_q/2\pi$ (GHz)	8.508	7.943
qubit anharmonicity $\alpha/2\pi$ (MHz)	-432	-357
qubit energy relaxation time T_1 (μs)	13.2	25.3
qubit echo dephasing time T_2 (μs)	10.4	15.9
ZZ interaction $\xi_{ZZ}/2\pi$ (MHz)	-0.73	-0.73
readout drive frequency $\omega_r/2\pi$ (GHz)	10.203	9.900
resonator dispersive shift $\chi/2\pi$ (MHz)	-1.4	-0.8
resonator external decay rate $\kappa_{ext}/2\pi$ (MHz)	6.3	4.5
readout error rate (%)	3.8	3.3
thermal excitation rate (%)	5.5	8.7

where $\langle \pm\sigma_x \rangle = 0$ for any n. Examples of the DRAG-weight calibration results are shown in Fig. 6(c). Figure 6(d) shows the pulse sequence to finely calibrate the pulse amplitude. In this sequence, we apply $(X_{\pi/2})^n$ to the initial state $|0\rangle$ and measure the ground-state population. The optimal pulse amplitude is the point where the ground-state population is 0.5 for any odd n.

APPENDIX C: COMPARISON WITH COMPOSITE PULSES

Composite pulses are known as a way to achieve quantum gates robust against systematic errors. Here we compare the performance between our optimal gate and a composite pulse family called compensation for off-resonance with a pulse sequence (CORPSE) [17] that is robust against detuning error.
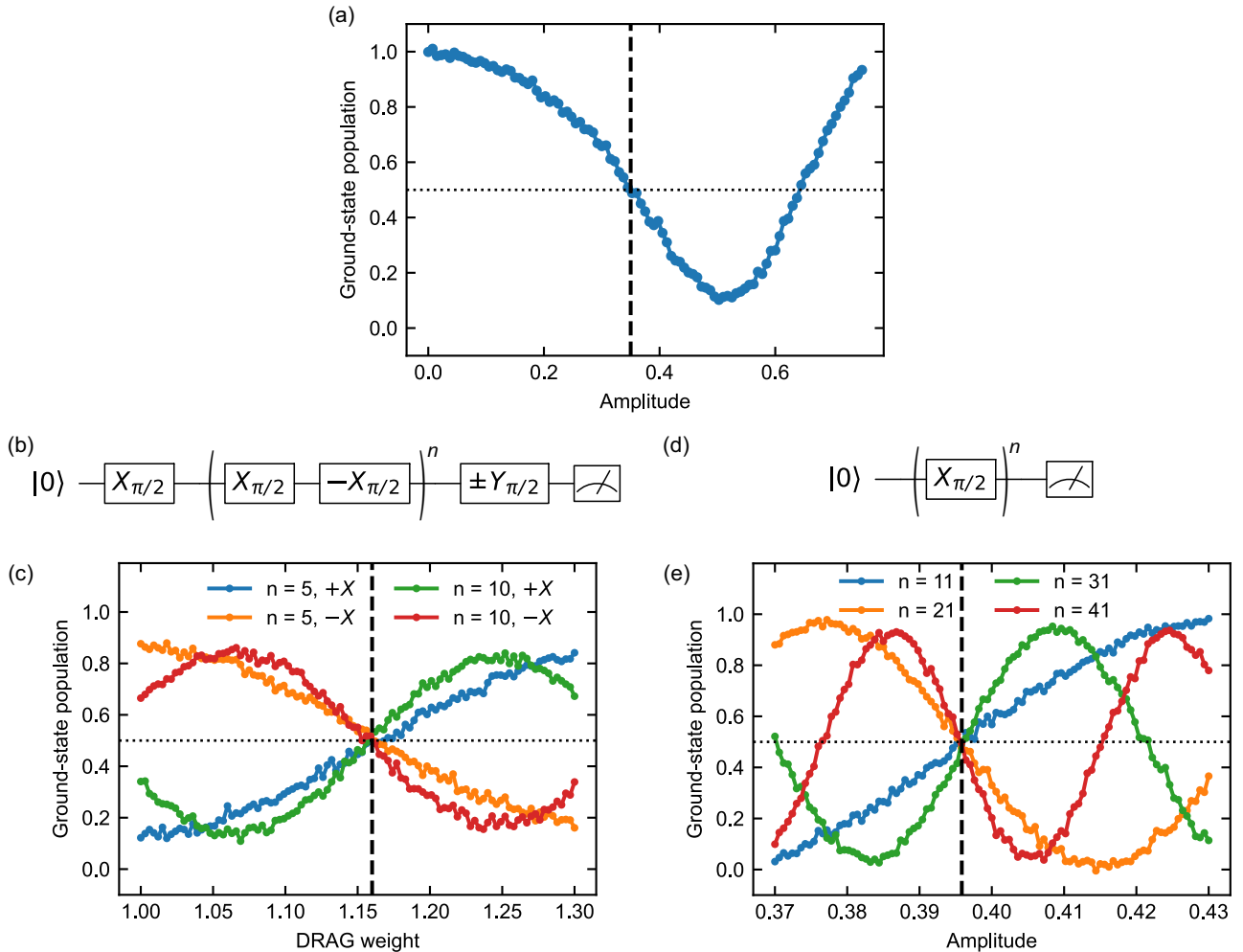

FIG. 6. Experimental calibration of the designed $X_{\pi/2}$ gate on Q0. (a) Rough estimation of the pulse amplitude. (b) Gate schematic and (c) the results of DRAG-weight calibration. (d) Gate schematic and (e) the results of pulse-amplitude calibration. The vertical dashed lines and the horizontal dotted lines in (a), (c), and (e) indicate the calibrated values and the ground-state population $P_g = 0.5$, respectively.
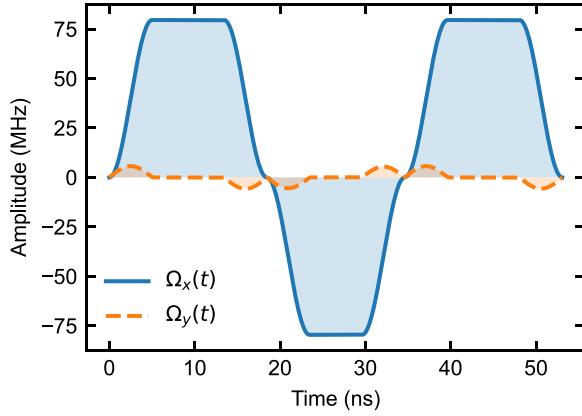
FIG. 7. Quadrature components of the waveform of the CORPSE $X_{\pi/2}$ gate with DRAG correction.

FIG. 8. Comparison of the $X_{\pi/2}$ gate in the robustness against the drive detuning with the CORPSE, optimal, and Gaussian pulses.

In general, CORPSE assumes that the individual pulses are rectangular shapes of equal amplitude. However, rectangular pulses are hard to execute because of the bandwidth limitation and the discontinuous turning on and off of the pulses. Here we instead utilize flat-top raised-cosine pulses to relax the sharp edges. This modification results in the deviation of the time evolution from the original theory and the reduction of the robustness. The rotation angles of the three pulses that construct the CORPSE X_θ gate are given by [17]

$$\theta_1 = 2n_1\pi + \frac{\theta}{2} - \arcsin\frac{\sin(\theta/2)}{2}, \quad \text{(C1)}$$

$$\theta_2 = 2n_2\pi - 2\arcsin\frac{\sin(\theta/2)}{2}, \quad \text{(C2)}$$

$$\theta_3 = 2n_3\pi + \frac{\theta}{2} - \arcsin\frac{\sin(\theta/2)}{2}, \quad \text{(C3)}$$

where n_1, n_2, and n_3 are integers, subject to the physical restriction that the resulting pulse angles must be positive. While choosing $n_1 = 1$, $n_2 = 1$, and $n_3 = 0$ is best since it minimizes remaining second-order error [17], such a choice makes the third pulse too short and experimentally impractical in terms of the adiabaticity. We thus choose $n_1 = n_2 = n_3 = 1$, which
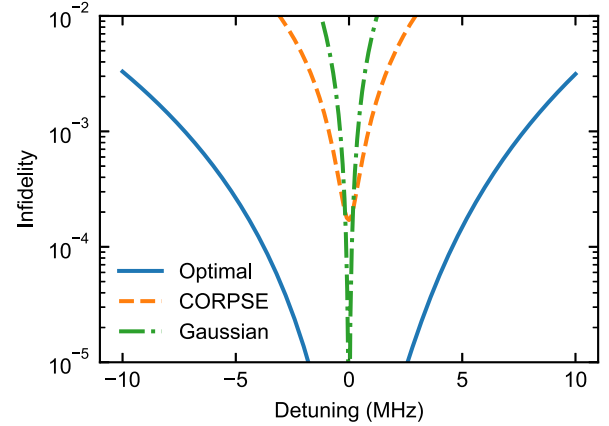
is still first-order insensitive against detuning error. The rotation angles of the three pulses that construct the CORPSE $X_{\pi/2}$ gate are given by $\{2.135\pi, 1.770\pi, 2.135\pi\}$ and pulse phases are $\{0, \pi, 0\}$, respectively. We set the rise-up and ring-down times to be 5 ns each. The maximum amplitudes of each pulse are the same as the optimal pulse used in the experiment. Figure 7 shows the waveforms of the CORPSE composite pulses. Each pulse includes numerically optimized DRAG correction. The comparison in robustness against the detuning error is shown in Fig. 8. Although the CORPSE composite pulse shows better robustness against detuning than the Gaussian pulse, the gate fidelity at zero detuning is orders of magnitude worse than the optimal and Gaussian pulses. This inferiority is due to the significant leakage error caused by the sharp edges and broad spectral distribution. If the rise-up and ring-down times of the flat-top pulses are made slower to reduce the leakage error, the advantage of the composite pulse is lost because the robustness is reduced. Therefore, the comparison made in this section highlights the advantage of our proposal over the composite pulse. Our method combines practicality in experimental applications with robustness against errors due to the careful choice of the waveform ansatz.

[1] S. Schlör, J. Lisenfeld, C. Müller, A. Bilmes, A. Schneider, D. P. Pappas, A. V. Ustinov, and M. Weides, Phys. Rev. Lett. **123**, 190502 (2019).

[2] B. G. Christensen, C. D. Wilen, A. Opremcak, J. Nelson, F. Schlenker, C. H. Zimonick, L. Faoro, L. B. Ioffe, Y. J. Rosen, J. L. DuBois, B. L. T. Plourde, and R. McDermott, Phys. Rev. B **100**, 140503(R) (2019).

[3] C. D. Wilen, S. Abdullah, N. A. Kurinsky, C. Stanford, L. Cardani, G. D'Imperio, C. Tomei, L. Faoro, L. B. Ioffe, C. H. Liu, A. Opremcak, B. G. Christensen, J. L. DuBois, and R. McDermott, Nature (London) **594**, 369 (2021).

[4] D. M. Tennant, L. A. Martinez, K. M. Beck, S. R. O'Kelley, C. D. Wilen, R. McDermott, J. L. DuBois, and Y. J. Rosen, PRX Quantum **3**, 030307 (2022).

[5] S. Diamond, V. Fatemi, M. Hays, H. Nho, P. D. Kurilovich, T. Connolly, V. R. Joshi, K. Serniak, L. Frunzio, L. I. Glazman, and M. H. Devoret, PRX Quantum **3**, 040304 (2022).

[6] A. Kandala, K. X. Wei, S. Srinivasan, E. Magesan, S. Carnevale, G. A. Keefe, D. Klaus, O. Dial, and D. C. McKay, Phys. Rev. Lett. **127**, 130501 (2021).

[7] P. Zhao, D. Lan, P. Xu, G. Xue, M. Blank, X. Tan, H. Yu, and Y. Yu, Phys. Rev. Appl. **16**, 024037 (2021).

[8] J. Stehlik, D. M. Zajac, D. L. Underwood, T. Phung, J. Blair, S. Carnevale, D. Klaus, G. A. Keefe, A. Carniol, M. Kumph, M. Steffen, and O. E. Dial, Phys. Rev. Lett. **127**, 080505 (2021).

[9] P. Mundada, G. Zhang, T. Hazard, and A. Houck, Phys. Rev. Appl. **12**, 054023 (2019).

[10] X. Xu and M. Ansari, Phys. Rev. Appl. **19**, 024057 (2023).

[11] Z. Ni, S. Li, L. Zhang, J. Chu, J. Niu, T. Yan, X. Deng, L. Hu, J. Li, Y. Zhong, S. Liu, F. Yan, Y. Xu, and D. Yu, Phys. Rev. Lett. **129**, 040502 (2022).

[12] K. X. Wei, E. Magesan, I. Lauer, S. Srinivasan, D. F. Bogorin, S. Carnevale, G. A. Keefe, Y. Kim, D. Klaus, W. Landers, N. Sundaresan, C. Wang, E. J. Zhang, M. Steffen, O. E. Dial, D. C. McKay, and A. Kandala, Phys. Rev. Lett. **129**, 060501 (2022).

[13] B. K. Mitchell, R. K. Naik, A. Morvan, A. Hashim, J. M. Kreikebaum, B. Marinelli, W. Lavrijsen, K. Nowrouzi, D. I. Santiago, and I. Siddiqi, Phys. Rev. Lett. **127**, 200502 (2021).

[14] C. Chamberland, G. Zhu, T. J. Yoder, J. B. Hertzberg, and A. W. Cross, Phys. Rev. X **10**, 011022 (2020).

[15] K. Khodjasteh and L. Viola, Phys. Rev. Lett. **102**, 080501 (2009).

[16] R. Tycko, Phys. Rev. Lett. **51**, 775 (1983).

[17] H. K. Cummins, G. Llewellyn, and J. A. Jones, Phys. Rev. A **67**, 042308 (2003).

[18] H. K. Cummins and J. A. Jones, New J. Phys. **2**, 006 (2000).

[19] B. T. Torosov and N. V. Vitanov, Phys. Rev. Appl. **18**, 034062 (2022).

[20] Y. Tabuchi, M. Negoro, and M. Kitagawa, Phys. Rev. A **96**, 022331 (2017).

[21] U. Haeberlen and J. S. Waugh, Phys. Rev. **175**, 453 (1968).

[22] A. R. R. Carvalho, H. Ball, M. J. Biercuk, M. R. Hush, and F. Thomsen, Phys. Rev. Appl. **15**, 064054 (2021).

[23] P. Rembold, N. Oshnik, M. M. Müller, S. Montangero, T. Calarco, and E. Neu, AVS Quantum Sci. **2**, 024701 (2020).

[24] N. H. Le, M. Cykiert, and E. Ginossar, npj Quantum Inf. **9**, 1 (2023).

[25] J. Werschnik and E. K. U. Gross, J. Phys. B **40**, R175 (2007).

[26] N. Khaneja, T. Reiss, C. Kehlet, T. Schulte-Herbrüggen, and S. J. Glaser, J. Magn. Reson. **172**, 296 (2005).

[27] N. Rach, M. M. Müller, T. Calarco, and S. Montangero, Phys. Rev. A **92**, 062343 (2015).

[28] D. M. Reich, M. Ndong, and C. P. Koch, J. Chem. Phys. **136**, 104103 (2012).

[29] W. Dong, F. Zhuang, S. E. Economou, and E. Barnes, PRX Quantum **2**, 030333 (2021).

[30] G. Dridi, K. Liu, and S. Guérin, Phys. Rev. Lett. **125**, 250403 (2020).

[31] J. Zeng, C. H. Yang, A. S. Dzurak, and E. Barnes, Phys. Rev. A **99**, 052321 (2019).

[32] D. Buterakos, S. Das Sarma, and E. Barnes, PRX Quantum **2**, 010341 (2021).

[33] U. Güngördü and J. P. Kestner, Phys. Rev. Res. **4**, 023155 (2022).

[34] X.-H. Deng, Y.-J. Hai, J.-N. Li, and Y. Song, arXiv:2103.08169

[35] Y.-J. Hai, J. Li, J. Zeng, D. Yu, and X.-H. Deng, arXiv:2210.14521.

[36] Y. Baum, M. Amico, S. Howell, M. Hush, M. Liuzzi, P. Mundada, T. Merkh, A. R. R. Carvalho, and M. J. Biercuk, PRX Quantum **2**, 040324 (2021).

[37] S. Sheldon, E. Magesan, J. M. Chow, and J. M. Gambetta, Phys. Rev. A **93**, 060302(R) (2016).

[38] N. Sundaresan, I. Lauer, E. Pritchett, E. Magesan, P. Jurcevic, and J. M. Gambetta, PRX Quantum **1**, 020318 (2020).

[39] P. Jurcevic, A. Javadi-Abhari, L. S. Bishop, I. Lauer, D. F. Bogorin, M. Brink, L. Capelluto, O. Günlük, T. Itoko, N. Kanazawa, A. Kandala, G. A. Keefe, K. Krsulich, W. Landers, E. P. Lewandowski, D. T. McClure, G. Nannicini, A. Narasgond, H. M. Nayfeh, E. Pritchett *et al.*, Quantum Sci. Technol. **6**, 025020 (2021).

[40] R. R. Ernst, G. Bodenhausen, and A. Wokaun, *Principles of Nuclear Magnetic Resonance in One and Two Dimensions* (Clarendon Press, Oxford, 1990).

[41] J. Nocedal, Math. Comput. **35**, 773 (1980).

[42] J. M. Gambetta, F. Motzoi, S. T. Merkel, and F. K. Wilhelm, Phys. Rev. A **83**, 012308 (2011).

[43] E. Magesan, J. M. Gambetta, and J. Emerson, Phys. Rev. Lett. **106**, 180504 (2011).

[44] E. Magesan, J. M. Gambetta, and J. Emerson, Phys. Rev. A **85**, 042311 (2012).

[45] D. C. McKay, C. J. Wood, S. Sheldon, J. M. Chow, and J. M. Gambetta, Phys. Rev. A **96**, 022330 (2017).

[46] A. S. Nikolaeva, E. O. Kiktenko, and A. K. Fedorov, Phys. Rev. A **105**, 032621 (2022).

[47] K. Luo, W. Huang, Z. Tao, L. Zhang, Y. Zhou, J. Chu, W. Liu, B. Wang, J. Cui, S. Liu, F. Yan, M.-H. Yung, Y. Chen, T. Yan, and D. Yu, Phys. Rev. Lett. **130**, 030603 (2023).

[48] K. Takeda, A. Noiri, T. Nakajima, T. Kobayashi, and S. Tarucha, Nature (London) **608**, 682 (2022).

[49] A. Noiri, K. Takeda, T. Nakajima, T. Kobayashi, A. Sammak, G. Scappucci, and S. Tarucha, Nature (London) **601**, 338 (2022).

[50] H. Ball, T. M. Stace, S. T. Flammia, and M. J. Biercuk, Phys. Rev. A **93**, 022303 (2016).

[51] M. Ganzhorn, G. Salis, D. J. Egger, A. Fuhrer, M. Mergenthaler, C. Müller, P. Müller, S. Paredes, M. Pechal, M. Werninghaus, and S. Filipp, Phys. Rev. Res. **2**, 033447 (2020).

[52] T. Tsunoda, G. Bhole, S. A. Jones, J. A. Jones, and P. J. Leek, Phys. Rev. A **102**, 032405 (2020).

[53] D. W. Leung, I. L. Chuang, F. Yamaguchi, and Y. Yamamoto, Phys. Rev. A **61**, 042310 (2000).

[54] J. A. Jones and E. Knill, J. Magn. Reson. **141**, 322 (1999).

[55] A. Parra-Rodriguez, P. Lougovski, L. Lamata, E. Solano, and M. Sanz, Phys. Rev. A **101**, 022305 (2020).

[56] C. J. Wood and J. M. Gambetta, Phys. Rev. A **97**, 032306 (2018).

[57] Z. Chen, J. Kelly, C. Quintana, R. Barends, B. Campbell, Y. Chen, B. Chiaro, A. Dunsworth, A. G. Fowler, E. Lucero, E. Jeffrey, A. Megrant, J. Mutus, M. Neeley, C. Neill, P. J. J. O'Malley, P. Roushan, D. Sank, A. Vainsencher, J. Wenner *et al.*, Phys. Rev. Lett. **116**, 020501 (2016).

[58] E. Jeffrey, D. Sank, J. Y. Mutus, T. C. White, J. Kelly, R. Barends, Y. Chen, Z. Chen, B. Chiaro, A. Dunsworth, A. Megrant, P. J. J. O'Malley, C. Neill, P. Roushan, A. Vainsencher, J. Wenner, A. N. Cleland, and J. M. Martinis, Phys. Rev. Lett. **112**, 190504 (2014).

[59] J. Y. Mutus, T. C. White, R. Barends, Y. Chen, Z. Chen, B. Chiaro, A. Dunsworth, E. Jeffrey, J. Kelly, A. Megrant, C. Neill, P. J. J. O'Malley, P. Roushan, D. Sank, A. Vainsencher, J. Wenner, K. M. Sundqvist, A. N. Cleland, and J. M. Martinis, Appl. Phys. Lett. **104**, 263513 (2014).

[60] T. Roy, S. Kundu, M. Chand, A. M. Vadiraj, A. Ranadive, N. Nehra, M. P. Patankar, J. Aumentado, A. A. Clerk, and R. Vijay, Appl. Phys. Lett. **107**, 262601 (2015).

[61] E. Lucero, J. Kelly, R. C. Bialczak, M. Lenander, M. Mariantoni, M. Neeley, A. D. O'Connell, D. Sank, H. Wang, M. Weides, J. Wenner, T. Yamamoto, A. N. Cleland, and J. M. Martinis, Phys. Rev. A **82**, 042339 (2010).